CFD Predictions of Fluctuating Pressure Environments on NASA's SLS Ascent Unsteady Aerodynamics Wind Tunnel Test

Jonathan Boustani*, Leslie Hall†
Mclaurin Aerospace, Jacobs Space Exploration Group, Huntsville, AL, 35802
Thomas B. Steva‡
NASA Marshall Space Flight Center, Huntsville, AL 35808

This paper details work that is being conducted on predicting fluctuating pressure environments on NASA launch vehicles using computational fluid dynamics (CFD). The accurate characterization of these aeroacoustic environments is necessary in the analysis of vehicle structural capability and development of subcomponent vibration design. High-fidelity simulations of the unsteady flow over NASA's SLS Ascent Unsteady Aerodynamics wind tunnel Test (AUAT) using the hybrid Reynolds-averaged Navier-Stokes (RANS)-large eddy simulations (LES) methodologies in Mississippi States' Loci/CHEM solver are presented. The two available methods, Nelson-Nichols and dynamic hybrid RANS-LES (DHRL), are compared head-to-head on identical grids at two Mach numbers. At the high-subsonic Mach number, locally supersonic flow expanding over a shoulder induces a separation-reattachment system that is predicted poorly by the Nelson-Nichols method due to an under-prediction in unsteady content. The DHRL solution predicts the spatial extent and frequency domain response of this system well but under-predicts the peak noise levels due to a delay in the RANS-to-LES transition. At the low-supersonic Mach number, compression corner dynamics dominate the unsteady flow. While the Nelson-Nichols solution captures this phenomenon well, another solution on a refined grid indicates that some model stress depletion is occurring. The DHRL solution again performs well at this Mach number and matches the wind tunnel data fairly closely, but perhaps most impressively, is fairly agnostic to increasing grid resolution. The findings in this paper are expected to be generally applicable and will be used to guide the prediction of aeroacoustic environments of other NASA launch vehicles.

I. Introduction

Unsteady flows and the pressure fluctuations that they create can affect the performance and integrity of vehicles in flight. Accurate characterization of the aeroacoustic environment and the identification of noise sources are then important steps in component and secondary structure vibroacoustic design. In the case of NASA launch vehicles, the Space Launch System (SLS) program has relied heavily on large-scale wind tunnel tests for developing aeroacoustic environments.[1] Over the last decade, however, strides in the field of computational fluid dynamics (CFD) have been making its use in the prediction of aeroacoustic environments more practical, both from improvements in hardware/speed-of-computation and algorithms/modeling.[2]

Perhaps the most critical flight regime is the transonic Mach number range. Locally supersonic flow over vehicle shoulders induces local flow separation and reattachment. This process generates significant fluctuating pressure levels (FPL). In the SLS program, the transonic regime contains the highest buffet environment on the vehicle, induced by a particularly tonal noise source which has received a high level of attention over the length of the program.[3,4] Furthermore, disturbances induced far upstream (*e.g.*, abort motor wakes) have been observed to convect along the length of the vehicle and affect the frequency content of downstream sources (*e.g.*, expansion-induced flow separation).[1]

From a CFD point-of-view, this introduces competing requirements that a numerical method be capable of acting robust enough to capture shocks while containing as little dissipation as possible so as to not artificially

*Aerospace Engineer, AIAA Member, jonathan.boustani@mclaurin.aero.
†Director of Engineering, AIAA Member
‡Aerodynamics Team Lead, Aerosciences Branch, AIAA Member

dampen the frequency content of flow features as they convect downstream. In addition to the convective considerations, external flows over launch vehicles are wall-bounded, and in applications considering 'real' engineering geometries and flow conditions, the high wavenumbers in the boundary layer prevent proper resolution of the energy cascade. Thus, the natural dissipation must be modeled. This removes direct numerical simulations (DNS) and wall-resolved large eddy simulations (WRLES) from consideration.

Wall-modeled LES (WMLES) is a promising strategy that, as the name implies, seeks to model the wall-stresses in the inner layer of the boundary layer while using LES methodologies to resolve the energetic eddies in the outer layer and other turbulent flow features (*e.g.,* regions of separated flow, vehicle wakes). The choice and design of the 'wall-stress model' itself is an area of active research that is beyond the scope of this paper but is summarized thoroughly by Larsson *et al.*[5] In perhaps its most simple form, the wall-model can be any Reynolds-averaged Navier-Stokes (RANS) turbulence model, also called hybrid RANS-LES. The transitioning between the RANS and LES regions is determined by a so-called shielding function. The function can be 'zonal', often user-defined at a constant height, or 'seamless', driven by the local grid spacing and solution.[5]

The present work will utilize multiple hybrid RANS-LES methodologies within Mississippi State's Loci/CHEM viscous Navier-Stokes solver[6,7] in order to simulate a few conditions from NASA's Ascent Unsteady Aerodynamics Test (AUAT). Both a transonic and a low-supersonic Mach number are considered. Emphasis is placed on comparison of FPL amplitudes and frequency content between different CFD solutions and available wind tunnel data, and effort will be made to explain observed differences as short-comings in the physical models or as spatial and temporal errors.

The present work proceeds as follows: Sec. II details the problem geometry and an overview of the surface and volume discretizations. Sec. III summarizes the numerical methodologies used in the CFD simulations. Sec. IV details results from CFD simulations compared with wind tunnel data before conclusions and items for future work are stated in Sec. V.

II. Problem Description

A. Geometry

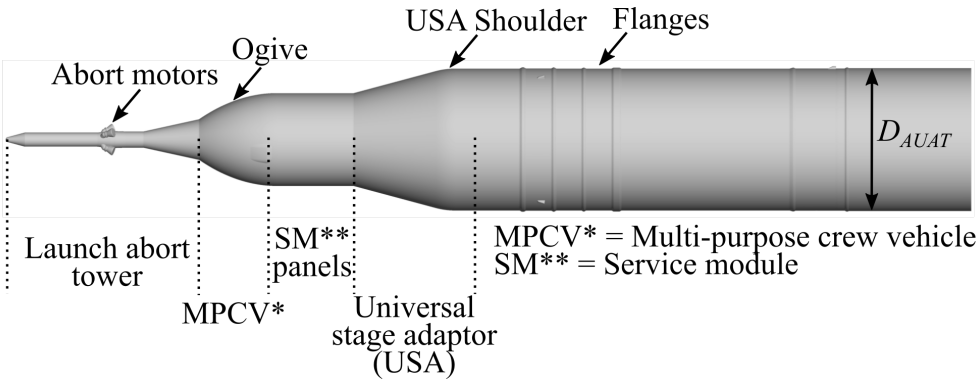

Figure 1: Annotated side-view of the 4%-scale SLS Block-1B forebody used in the current work.

NASA's SLS Ascent Unsteady Aerodynamics Wind Tunnel Test (AUAT) was the second of two test campaigns conducted at the Ames Unitary Plan Wind Tunnel with the goal of characterizing SLS unsteady environments. While the AUAT tests considered multiple SLS variants, the outer-mold-line (OML) considered in the present work is a 4%-scale 28000-configuration SLS Block-1B forebody (see Fig. 1). This model includes multiple protuberances in the form of cameras, flanges, and an MPCV umbilical plate. Note that the model sting is not considered nor are the wind tunnel walls. Any differences arising between wind tunnel and 'free-air' conditions (*e.g.,* tunnel tones, blockage) are then not quantified or considered here.

B. Fluid domain

1. Surface Mesh

The use of triangular surface meshes, and thus tetrahedral-dominant volume meshes, when using unstructured solvers is incredibly common due to the ease of generating triangular discretizations for arbitrarily complex geometries. This is the same reason triangular surface meshes are commonly used in simulations involving Immersed Boundary Methods (IBM), which by design are adept at handling complex geometries.[8–10] In addition, without complex treatment, second-order spatially-accurate operators are easily constructed on these 'fully-unstructured' grids. As will be elaborated on in Sec. III, however, the higher-order spatially-accurate and

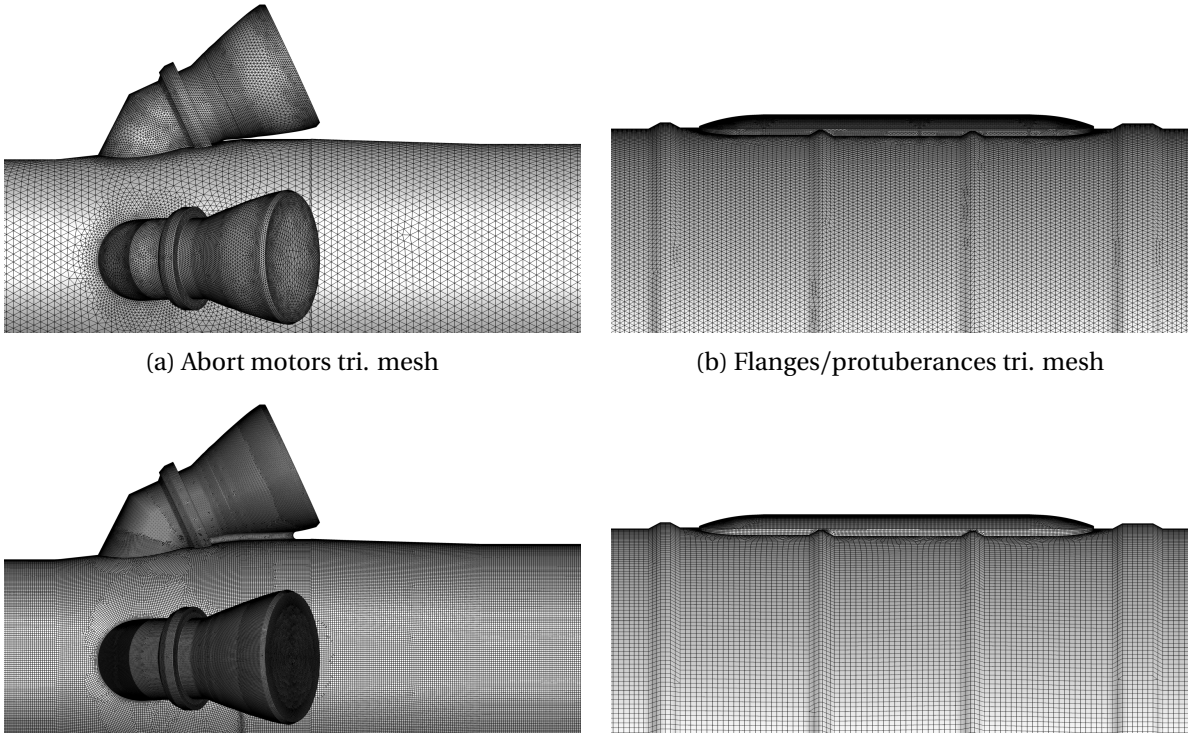

(a) Abort motors tri. mesh

(b) Flanges/protuberances tri. mesh

(c) Abort motors quad. mesh

(d) Flanges/protuberances quad. mesh

Figure 2: Zoomed-in view of the surface mesh on the abort motors and flanges/protuberances for the medium triangular surface mesh (top row) and quadrilateral surface mesh (bottom row).

low-dissipation algorithms in Loci/CHEM benefit from and often times require a more structured grid, be it curvilinear or Cartesian.[11] Thus, only quadrilateral-dominant surface meshes (and hexagonal-dominant volume meshes) are used in the simulations in the present work, but a counterpart triangular/tetrahedral mesh is considered through this section and the next to further illustrate this motivation. Both surface meshes are generated with ANSA Preprocessor©, developed by BETA-CAE Systems. In the case of the quadrilateral surface mesh, the use of some (<1%) triangular elements is necessitated in regions of high convexity. Zoomed-in views of the 'medium' surface meshes on the abort motors (AMs) and near flanges and a protuberance on the core stage are shown for both mesh types in Fig. 2. Each mesh type is considered at two levels of resolution. In this paper, these will be referred to as the 'medium' and 'fine' meshes, corresponding to a nominal edge length of 2.54mm and 1.27mm over the majority of the vehicle, respectively.

2. Volume Mesh

In order to generate a volume mesh from the triangular surface discretization, Mississippi State's AFLR3[12,13] is employed. AFLR3 generates hybrid unstructured grids that are generally tetrahedral-dominant unless otherwise specified. For the quadrilateral surface mesh, ANSA Preprocessor© is used to generate predominantly-hexagonal cells, and user-defined constraints are designed to create a uniformly-spaced, isotopic region near the wall that

mimics a Cartesian grid. These unit aspect ratio cells are desirable in the regions of flow where the LES scheme is expected to be active,[5,14] and Loci/CHEM's low-dissipation convective scheme performs best on a structured or Cartesian/hexagonal grid.[11] Both volume meshes grow inflation layers off of the no-slip surfaces with a first cell height at a y^+ value of 1 corresponding to the considered freestream conditions. Note that in the version of ANSA Preprocessor© that was used to generate the hexagonal volume mesh, the 'top' of the growing inflation layer could not intersect itself, and thus, some compromise in the underlying geometry under the AMs was necessary for this grid (compare Fig. 2c to Fig. 2a), but this change is assumed to be insignificant to the overall flow.

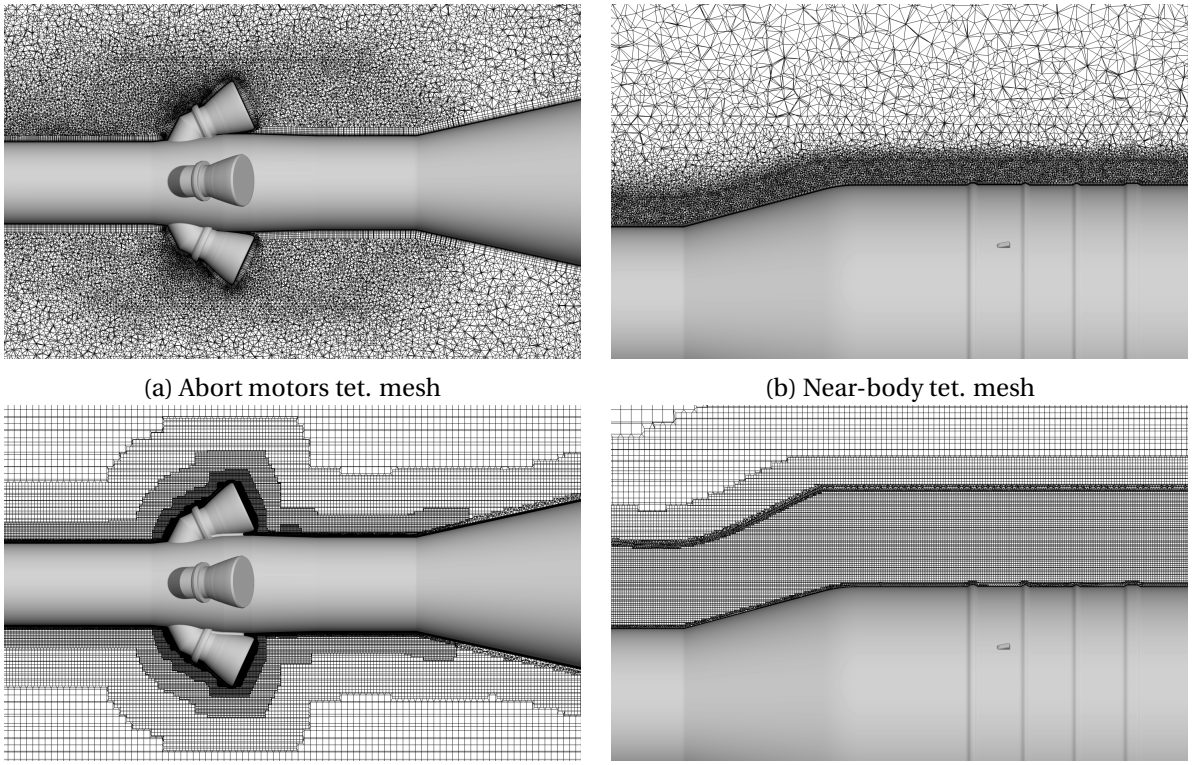

(a) Abort motors tet. mesh

(b) Near-body tet. mesh

(c) Abort motors hex. mesh

(d) Near-body hex. mesh

Figure 3: Slices of the medium tetrahedral-dominant (left) and hexagon-dominant (right) volume meshes near the abort motors and flanges.

Slices through the tetrahedral- and hexagonal-dominant volume domains are shown in Fig. 3. Both volume meshes are refined heavily near the abort motors and maintain a region of uniformly-refined cells in the near-wall region that matches the surface resolution. As the tetrahedral mesh moves away from the body, the cells simply get larger. To avoid split-faces in the hexagon mesh, however, the different 'levels' of hexagonal cells are connected by a rim of transitional pyramidal and pentagonal cells. Slices of the entire computational domain for each mesh type are shown in Fig. 4.

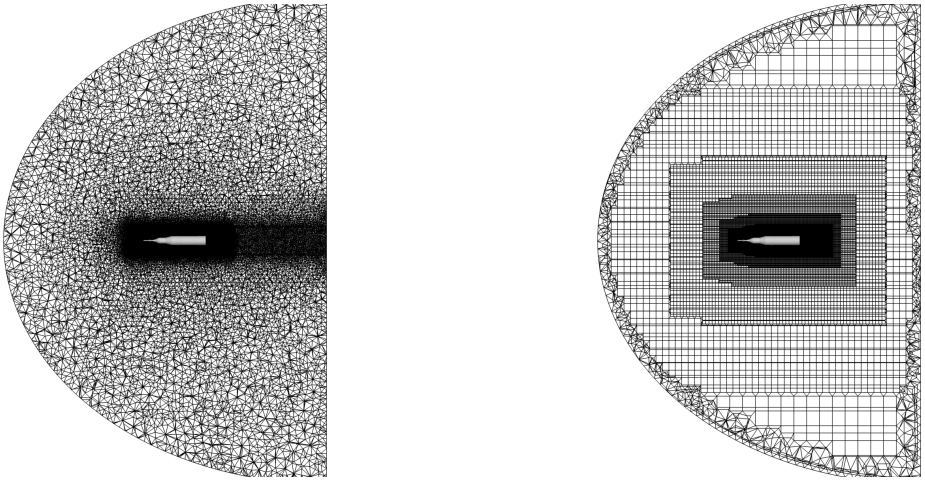

(a) (b)

Figure 4: Slices of the mesh through the (a) tet. and (b) hex. volume domains.

III. Numerical Methods

All simulations are performed using second-order time-accurate implicit backward-differentiation within Mississippi State's Loci/CHEM viscous Navier-Stokes solver.[6,7] The contradicting demands of being robust at shocks but providing low dissipation in smooth regions of flow are met by using Loci/CHEM's low-dissipation solver.[11] In this solver, a low-dissipation Roe scheme is blended with fourth-order spatially-accurate skew-symmetric flux. The switch to Roe is only allowed in regions of highly-compressible flow such as shocks and expansions, thus, to maintain stability in smooth regions, some user-defined amount of third-order upwind flux is always present. The always-present third-order upwinding also acts an implicit filter for large eddy simulations (LES), damping waves with sufficiently high wavenumbers across the entire domain. Third-order upwinding is also added when 'non-ideal' meshes are used, or when the local mesh deviates from a Cartesian-alignment, as the skew-symmetric scheme is expecting a symmetric stencil. This deviation from Cartesian-alignment is measured by $0 \leq \alpha_{geom.} \leq 1$, where $\alpha_{geom.} \approx 0$ represents excellent Cartesian-alignment and $\alpha_{geom.} \approx 1$ represents poor alignment. This is the motivation for considering the hexagonal volume mesh as an alternative to more standard 'fully-unstructured', tetrahedral-dominant meshes when conducting simulations with the low-dissipation solver in the present work. This is further illustrated in Fig. 5, where contours of $\alpha_{geom.}$ for the tetrahedral and hexagonal volume meshes are shown on cut-planes through the volume domain. Morris and Luke provide further details on the numerical formulation of the low-dissipation solver that are beyond the scope of the current effort.[11]

A. Wall Treatment

The decay of energetic eddies in the inner boundary layer are modeled with Mentor's Baseline Model (BSL).[15] Thus, in the terminology specified by Larsson *et al.*,[5] the simulations are conducted in a 'wall-modeled' LES fashion, and more specifically, with a RANS model acting as the wall-model. The outer layer dynamics and regions of separated flow are resolved using the aforementioned (implicit) LES strategy. The transition from the RANS region to the LES region inside the code is handled by a so-called 'shielding function', the form of which varies from method to method.

1. Nelson-Nichols Hybrid RANS-LES

Loci/CHEM has two hybrid RANS-LES methods - the more simple of the two being the hybrid RANS-LES approach by Nelson and Nichols.[16] In this method, an estimate of the local turbulent length scale, $L_T = k^{1/2}/\omega$, is compared against the local grid spacing, L_G. If the ratio of the two is sufficiently high, its determined that there is enough resolution to resolve the turbulent energy, and the eddy viscosity is set to be an 'LES' eddy viscosity.[16]

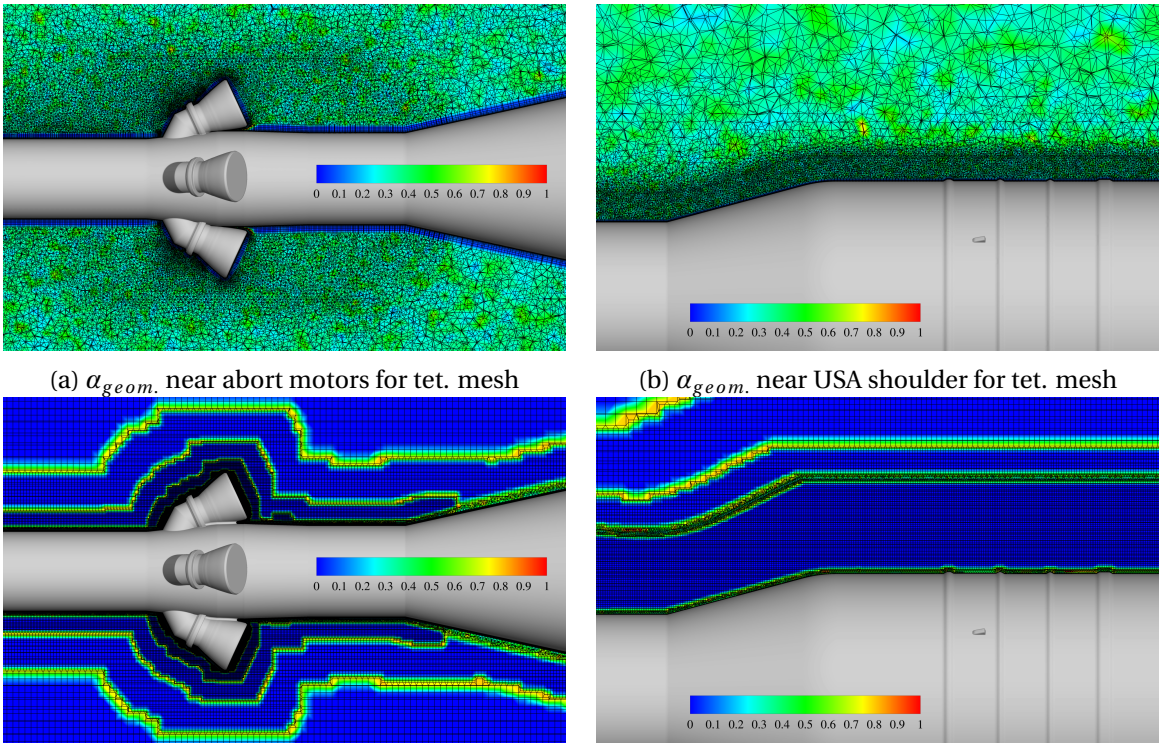

(a) $\alpha_{geom.}$ near abort motors for tet. mesh

(b) $\alpha_{geom.}$ near USA shoulder for tet. mesh

(c) $\alpha_{geom.}$ near abort motors for hex. mesh

(d) $\alpha_{geom.}$ near USA shoulder for hex. mesh

Figure 5: Pseudocolor contours of $\alpha_{geom.}$ shown on a cut-plane through the center of the domain for the medium tetrahedral-dominant (top) and hexagonal-dominant (bottom) meshes.

If the ratio is sufficiently small, the eddy viscosity is directly provided by the turbulence model. Once this ratio is expressed as a smooth and continuous function, Λ, the shielding function, f_d, can be defined as

$$f_d = \frac{1}{2}\Big(1+\tanh(2\pi(\Lambda-0.5))\Big) \tag{1}$$

where

$$\Lambda = \frac{1}{1+\left(\frac{L_T}{2L_G}\right)^{4/3}} \tag{2}$$

These equations are then used to define a blended turbulent eddy viscosity that is of the form

$$\nu_t = \nu_{t,RANS} f_d + (1-f_d)\nu_{t,LES)} = \nu_{t,RANS} f_d + (1-f_d)\min\Big(0.0854 L_G \sqrt{f_d k_{RANS}}, \nu_{t,RANS}\Big). \tag{3}$$

Note that this method solves RANS on the instantaneous flow field quantities. Due to the simplicity of the shielding function, the method may suffer from model stress depletion (MSD) when sufficiently refined grids are used and/or the turbulent kinetic energy is not large enough to prevent the LES region from penetrating into the inner regions of the boundary layer. This would manifest as a dramatic drop in shear stresses at the wall and excessive separation.

2. *Dynamic Hybrid RANS-LES*

The second hybrid RANS-LES approach in Loci/CHEM is so-called 'dynamic' hybrid RANS-LES (DHRL) by Bhushan and Walters[17] and Walters *et al.*[18] This method, similar to that of Nelson and Nichols, can couple any RANS method with any LES approach (sub-grid scale model or implicit filtering). At the core of the DHRL shielding function is the comparison of resolved production of turbulent kinetic energy to that predicted by the chosen RANS and LES models. That is,

$$\alpha = \frac{-\overline{u_i'' u_j''}\overline{S}_{ij}}{\tau_{ij}^{RANS}\overline{S}_{ij} - \overline{\tau}_{ij}^{SGS}\overline{S}_{ij}}, \tag{4}$$

where u_i'' represents components of the resolved fluctuating velocity, τ_{ij}^{RANS} and τ_{ij}^{SGS} represent the sub-grid stresses predicted by a chosen RANS and sub-grid stress/LES model, and $\overline{S}_{ij}$ represents components of the rate of strain tensor. Overbars denote Favre-averaged variables. The term in the numerator represents the resolved production, the first term in the denominator represents RANS-predicted production, and the second term in the denominator represents production predicted by the sub-grid scale model. For the implicit LES approaches used here, this term is zero. This can be used to define a shielding function for stress of the form

$$\tau_{ij} = \alpha\tau_{ij}^{SGS} + (1-\alpha)\tau_{ij}^{RANS}. \tag{5}$$

More details on how the Favre-averaged and RANS variables are computed and how the DHRL method is applied to turbulent heat flux can be found in Refs. 17 and 18, but the general idea is that RANS is solved on a continuously Favre-averaged flow field. An unpublished modification to DHRL is also available in Loci/CHEM that addresses short-comings that the original formulation has in the prediction of turbulent heat flux and the dependence on the chosen RANS model. The latter of these two modifications is briefly explained here.

It is typically the case that a hybrid RANS-LES method 'inherits' the short-comings of the chosen RANS model. For example, in the case of DHRL, in regions where a RANS model alone would over-predict Reynolds stresses, the DHRL model would as well, even if the LES in that region is sufficiently well-resolved, simply due to the definition of the shielding function. In the modified DHRL formulation, the shielding function is then made to be the maximum of the original α parameter and a new γ parameter that represents time-scales in the problem at hand:

$$\gamma = 1 - \left[1 + \left(\frac{\varsigma}{\varsigma_c}\right)^m\right]^{-1} \tag{6}$$

where ς_c and m are constants (usually both are 2) and

$$\varsigma = \frac{\overline{S_{ij}S_{ij}} - \overline{S_{ij}}\,\overline{S_{ij}}}{\overline{S_{ij}}\,\overline{S_{ij}}}. \tag{7}$$

The variable ς is introduced such that it trends towards zero for steady flows and is much larger than unity for unsteady flows. Thus, a final modified shielding function for shear stress can be written as

$$\tau_{ij} = \alpha_{eff.}\tau_{ij}^{SGS} + (1-\alpha_{eff.})\tau_{ij}^{RANS} \tag{8}$$

where $\alpha_{eff.} = \max.(\alpha, \gamma)$. The end result of this is a shielding function that operates in pure LES mode in regions of highly-resolved separated flow. When within an attached turbulent boundary layer, the method will operate in 'DHRL mode', where the shielding function is solely chosen by α. The modified methodology is the one used in the present work, and readers interested in further details are referred to the developers of Loci/CHEM and the DHRL model.

IV. Results

Results from the two hybrid RANS-LES strategies are obtained for two Mach number conditions from the AUAT test schedule. That is, $M = 0.84$, characterized by a prominent expansion-induced flow separation and reattachment just downstream of the USA shoulder, and $M = 1.1$, which is characterized by conventional compression corner dynamics on the USA windward-angled surface. Due to export restrictions, all results are shown here without values on most of the axes, though meaningful insight between the CFD predictions and available wind tunnel data will still be clearly presented.

A. Case 1: $M = 0.84$

The hybrid RANS-LES simulations are initialized with a steady-state RANS solution that is advanced with a local-time stepping algorithm until integrated forces and probe pressures reach a statistically-stationary or converged

limit. Furthermore, the RANS solution is probed for the maximum velocity in the expected LES-region, *i.e.*, within the isotropic grid cells in the near-wall region (see Fig. 2d). This velocity is combined with the medium grid's near-wall spacing of $0.1in$ and the suggestion of $\mathrm{CFL}_{max} \approx 1$ (see Ref. 14) in the LES region to obtain a global timestep of $\Delta t = 6.35\times10^{-6}s$ for the coming LES simulations. Fig. 6 shows contours of CFL number on a cut-plane through the center of the domain at an instance in time from the DHRL simulation. The CFL number is always less than 1 in the LES regions with a maximum value of 1 occurring in the expansion. Once the LES simulations are started from the RANS flowfield, sufficient time is allowed to convect any transients out of the domain before statistics are sampled, generally about 20-30 convective-time-units (CTU) when computed with the length of the AUAT geometry and the freestream velocity. The statistics are sampled over $1s$ of physical time, or, about 158000 timesteps (approximately 117 CTUs).

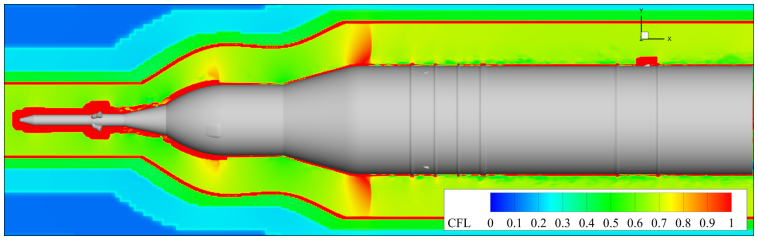

Figure 6: Contours of local CFL number shown on a cut-plane through the center of the domain obtained from an instance in time during the $M = 0.84$ DHRL simulation.

1. *Flow Visualization*

Fig. 7 shows contours of Mach number and numerical shadowgraphs for both of the hybrid RANS-LES solutions conducted at $M = 0.84$. The hybrid RANS-LES cases show clear resolution of unsteady eddies in the near body region, especially just downstream of the abort motors and of the expansion-induced separation that manifests over the shoulder of the USA. Closer inspection indicates that the size of the eddies near the body may be smaller and better resolved by DHRL when compared to Nelson-Nichols.

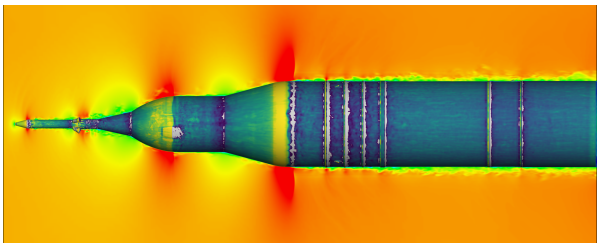

(a) DHRL, Mach number and $c_{f,x}$

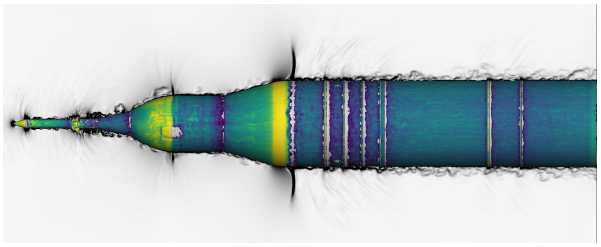

(b) DHRL, $||\nabla\rho||$ and $c_{f,x}$

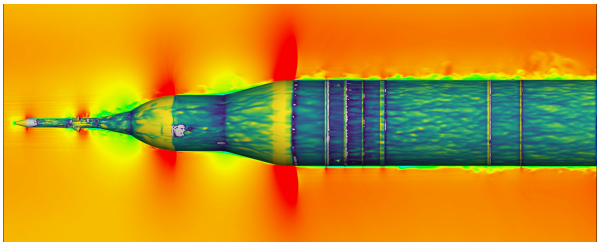

(c) Nelson-Nichols, Mach number and $c_{f,x}$

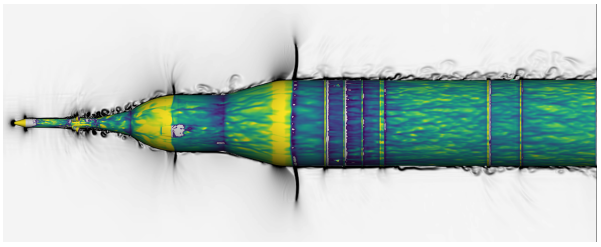

(d) Nelson-Nichols, $||\nabla\rho||$ and $c_{f,x}$

Figure 7: Saturated pseudocolor contours of Mach number (left column) and magnitude of density gradient (right column) shown on a cut-plane through the center of the domain at an instance in time from the DHRL and Nelson-Nichols HRLES simulations conducted at $M = 0.84$. Surface contours of skin friction coefficient 'blanked' for values less than zero are also shown on the body.

Looking at the surface contours of $c_{f,x}$ in Fig. 7, which because of the value blanking, is not present for values less than zero, its clear that the DHRL solution predicts more separation downstream of the USA shoulder than the Nelson-Nichols method, which appears to stay attached over majority of the body. This is an early indication that the shielding functions from DHRL and Nelson-Nichols are responding in different manners to the expansion-induced separation over the shoulder. It is also an indication that for the case of Nelson and Nichols HRLES, the amplitude of the pressure fluctuations in this area may show large disagreement with wind tunnel data. Despite this, all methods predict at least some level of separation as the expanded flow reaches the circumferential flanges downstream of the USA.

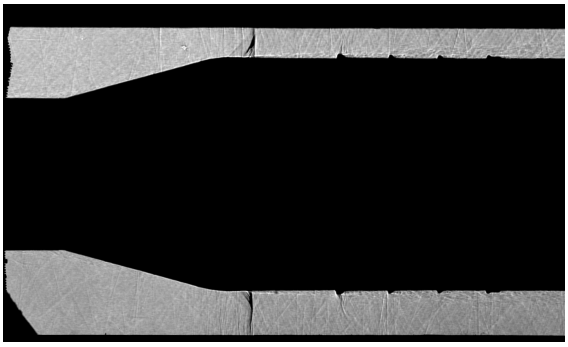

(a) Wind tunnel shadowgraph

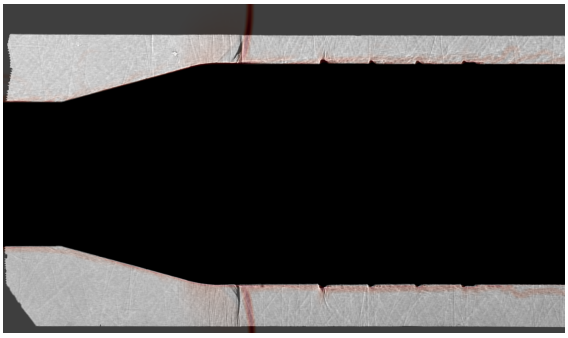

(b) Nelson-Nichols hybrid RANS-LES solution

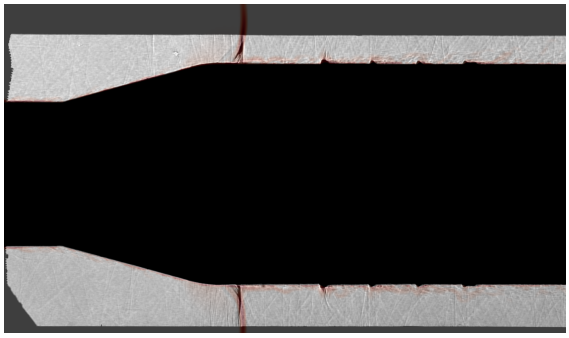

(c) DHRL solution

Figure 8: (a) Original wind tunnel shadowgraph and (b)-(c) semi-transparent wind tunnel shadowgraph overlaid on numerical shadowgraphs from the $M = 0.84$ Nelson-Nichols hybrid RANS-LES and DHRL solutions. Note that the numerical shadowgraphs from the CFD solutions are presented with a white-red color map while the wind tunnel shadowgraph is presented in grey-scale.

Fig. 8 shows semi-transparent shadowgraphs originally obtained during the AUAT wind tunnel testing overlaid on the two hybrid RANS-LES solutions from the current work. The CFD shadowgraphs in the background of the images are shown on a white-red color map to contrast the grey-scale used in the wind tunnel. Inspection of Fig. 8b indicates that the solution predicted by the Nelson and Nichols HRLES method fails to capture the location and shape of the expansion-induced normal shock. This is most obvious when looking at the underside of the vehicle in the figure. In contrast, the DHRL solution shown in Fig.8c captures the location and shape of the normal shock well. In addition, there is an obvious breakup of the larger flow features immediately off the wall into smaller features in the DHRL solution that is not present in the solution from Nelson and Nichols. This is also expected to affect not only the spatial extent of the separation region aft of the shock but also the intensity and frequency content of the surface pressure fluctuations.

2. RMS Sound Pressure

The CFD simulations were set up with 250 'probed' locations on the surface of the geometry that correspond to the location of Kulite® pressure transducers present on the AUAT wind tunnel model. These probed locations,

simply referred to as 'probes' here, sampled the flow field at each timestep during the course of the CFD simulation. Note that only the statistically stationary portion of the total time signal is used for analysis here.

The analysis starts with a coarse look at the spatial distribution of the pressure fluctuations over the entire surface. Surface data was not saved at every timestep, however, so in order to consider the entire computed frequency range, data defined at the probe locations is interpolated using simple nearest-neighbor logic to the centroids of elements on a very under-resolved mesh of the AUAT geometry. Fig. 9 shows the interpolated overall sound-pressure-level (OASPL),

$$\text{OASPL}\,(dB) = 20\log_{10}\left(\frac{P_{rms}}{P_{ref.}}\right),\ P_{ref} = 2.90075\times10^{-9}psi, \tag{9}$$

obtained from post-processing of the wind tunnel data (Fig. 9a) and the two CFD simulations (Figs. 9b-9c) and the differences between the wind tunnel data and CFD simulations (Figs. 9d-9e).

Fig. 9a clearly shows the expansion-induced separation and reattachment system occurring on the USA shoulder. Downstream of this, the flow interacts with several circumferential flanges that causes additional regions of locally separated flow. These phenomena produce spikes in OASPL that are indicated by the yellow/orange/red contours. While DHRL qualitatively captures the separated flow region aft of the shoulder separation and within the flange region (as indicated by Figs. 9c and 9e), the Nelson-Nichols solution shows much lower values of OASPL relative to the wind tunnel. Most notably, the separation and reattachment system occurring just aft of the USA shoulder normal shock is virtually non-existant in the Nelson-Nichols solution, and the OASPL only slightly rises as the expanded flow reaches the circumferential flanges.

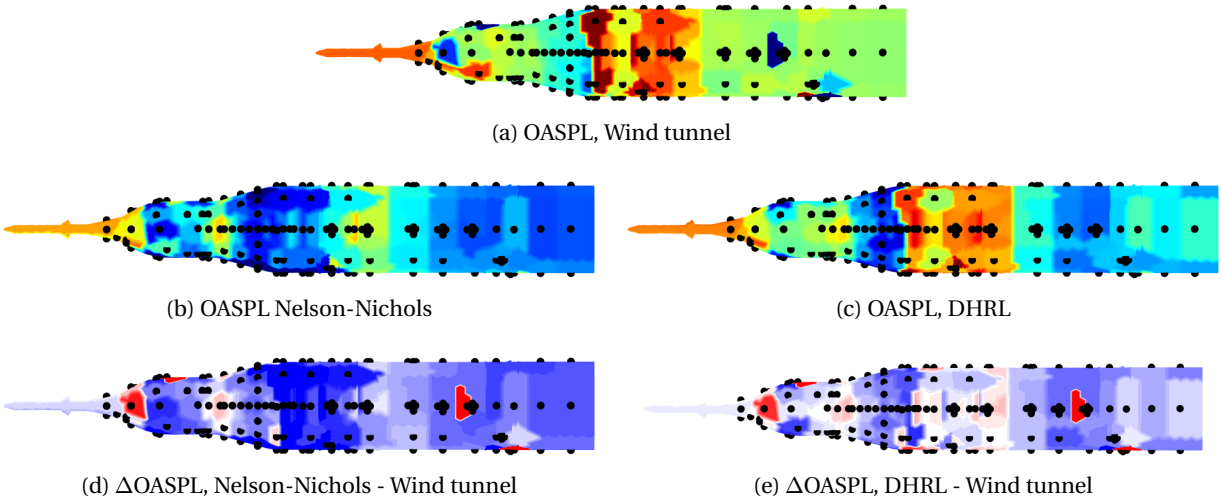

(a) OASPL, Wind tunnel

(b) OASPL Nelson-Nichols

(c) OASPL, DHRL

(d) ΔOASPL, Nelson-Nichols - Wind tunnel

(e) ΔOASPL, DHRL - Wind tunnel

Figure 9: Contours of OASPL interpolated from Kulite® locations to the centroids of surface elements on a coarse AUAT mesh for the $M = 0.84$ (a) wind tunnel data, (b) Nelson-Nichols CFD solution, and (c) DHRL CFD solution shown in the $x-y$ plane. Images (d) and (e) show the interpolated values of ΔOASPL, indicating the difference between the CFD predictions and wind tunnel measurements of OASPL.

Its worth noting that even in regions that should be 'quiet', *e.g.*, the flow expanding over the ogive of the MPCV and the attached flow region downstream of the circumferential flanges, the 'floor' of the wind tunnel OASPL values is notably higher than that from the CFD solutions. The current rationale for this is that the AUAT wind tunnel tests were not conducted in a 'quiet' tunnel – as opposed to the CFD simulations that are conducted in 'free-air', and contain essentially zero ambient noise. When a flow feature such as the separation-reattachment system on the USA shoulder can produce OASPL levels that are 'louder' than the tunnel background noise, this effect is not noticed. In quiet regions, however, the tunnel background noise generally elevates the baseline OASPL levels that would otherwise be measured.

The root-mean-square (RMS) of the pressure coefficient, $c_{p,rms}$, is now compared at the Kulite® locations in order to measure how well the CFD simulations predict the level of pressure fluctuations at the discrete probe locations. This will be conducted along several roll/clocking-angles (see Fig. 10 for an illustration of the definition of positive clocking-angle and notable values). It may become important to note that in Loci/CHEM, the probes

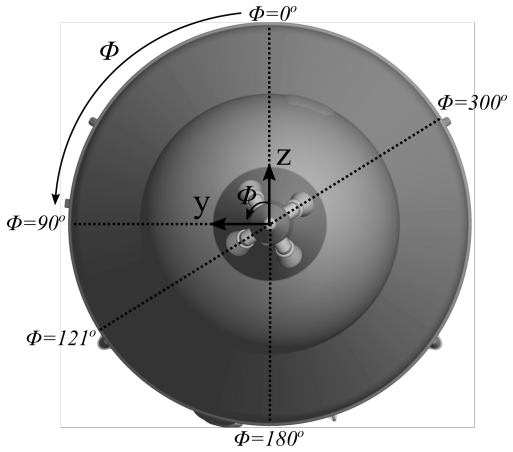

Figure 10: Definition of roll/clocking-angle used in the present work. Also included are notable clocking-angles where majority of the presently considered data is obtained from.

are not sampled at the exact user-specified location but at the center of the closest surface element, creating a potential $\mathcal{O}(\Delta x)$ error in the data sampled at the probe.

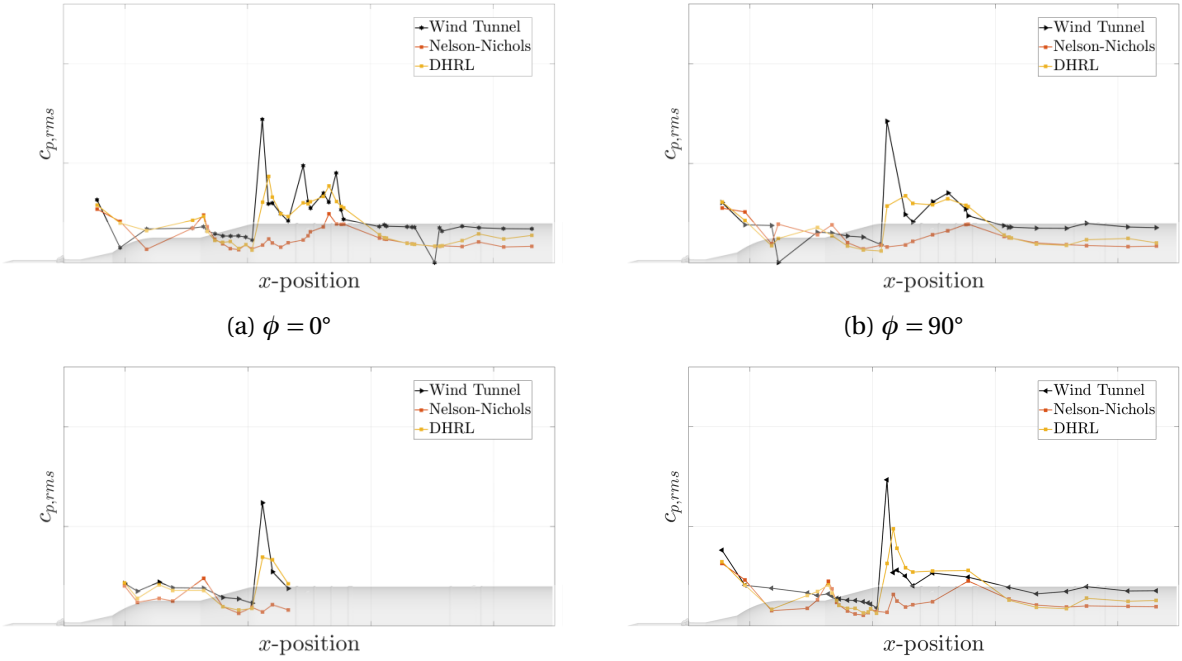

(a) $\phi = 0°$ (b) $\phi = 90°$

(c) $\phi = 121°$ (d) $\phi = 180°$

Figure 11: Plots of $c_{p,rms}$ versus x-coordinate along various constant clocking-angles for the $M = 0.84$ case.

Consistent with what has been shown so far, the solution predicted by the Nelson-Nichols method fails to capture any rise in pressure fluctuations in the USA shoulder separation-reattachment system, seeing only a minor rise by the time the flow reaches the flanges. On the other hand, while the DHRL solution has thus far shown good qualitative agreement with the wind tunnel data in terms of predicting the general level and spatial extent of regions with elevated pressure levels, we now see that the DHRL-predicted USA shoulder reattachment noise levels are actually lower than the wind tunnel data. The DHRL prediction of the pressure levels over the flanges, however, is generally good throughout the region, with local differences occurring on a probe-by-probe basis. One encouraging finding is that the agreement for the 'first', or left-most, data point in each plot shows

great agreement between both CFD predictions and the wind tunnel. This data point is directly influenced by the region of massively separated flow in the wake of the abort motors, especially in the case of Fig. 11c, where the clocking-angle is directly behind one of the abort motors. In this region, there is little ambiguity about whether the CFD solution should be acting in RANS- or LES-mode due to the massive flow separation. The smooth-body separation over the USA shoulder, however, is a much more difficult problem worth further investigation.

It was first hypothesized that the normal shock occurring downstream of the USA shoulder may sit in a slightly different location in the CFD simulations compared to the wind tunnel due to tunnel versus free-air effects. Even a small difference in the location of the shock foot may cause the discrete probe location to 'miss' the reattachment since the probe represents only a single point in space. To test this hypothesis, and to simultaneously reduce the effect of the potential $\mathcal{O}(\Delta x)$ sampling error, new probe locations were prescribed along several clocking-angles with the streamwise spacing of the probes set equal to the streamwise spacing of the surface mesh elements. The previous plots of $c_{p,rms}$ versus x-coordinate from Fig. 11 are reproduced in Fig. 12 with an additional curve representing the DHRL solution being restarted and allowed to run for 25 additional CTUs with the new probe locations. Along the clocking-angles of $\phi = 0°$ and $\phi = 180°$, the peak in $c_{p,rms}$ occurring in the USA separation-reattachment system is not any better resolved, though at $\phi = 90°$ and $\phi = 121°$, there is an appreciable increase in $c_{p,rms}$ and strong indication that the reattachment was already predicted at the correct point in space. Despite this, the predicted peak in $c_{p,rms}$ does not reach the wind tunnel data, and further analysis is required. Of note, however, are the even larger spikes in $c_{p,rms}$ near the circumferential flanges. It appears both the original CFD probes and the wind tunnel Kulites® 'miss' the maximum values of $c_{p,rms}$ due to the spatial resolution provided by the sensors.

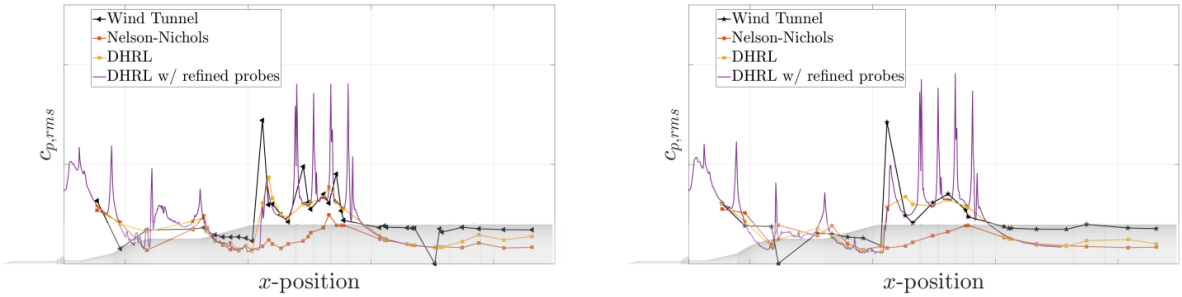

(a) $\phi = 0°$ (b) $\phi = 90°$

(c) $\phi = 121°$ (d) $\phi = 180°$

Figure 12: Plots of $c_{p,rms}$ versus x-coordinate along various constant clocking-angles with an additional curve representing a restarted DHRL solution with a dense line of probes defined with a streamwise spacing equal to the surface mesh spacing.

The shielding function is evaluated next. While primarily the DHRL solution is under scrutiny here, it is instructive to compare the shielding function for both methods. It is known that one common flaw of hybrid RANS-LES strategies is the delay in the formation of 'LES-content' or flow instabilities due to downstream convection RANS-levels of eddy viscosity and/or a slow response of the shielding function.[19] The under-prediction of the fluctuating pressure levels aft of the USA normal shock in the DHRL case could be due to the shielding function not responding quick enough or becoming corrupted by the upstream RANS eddy viscosity. The shielding functions for both HRLES methods are shown on a cut-plane through the center of the domain in Fig. 13.

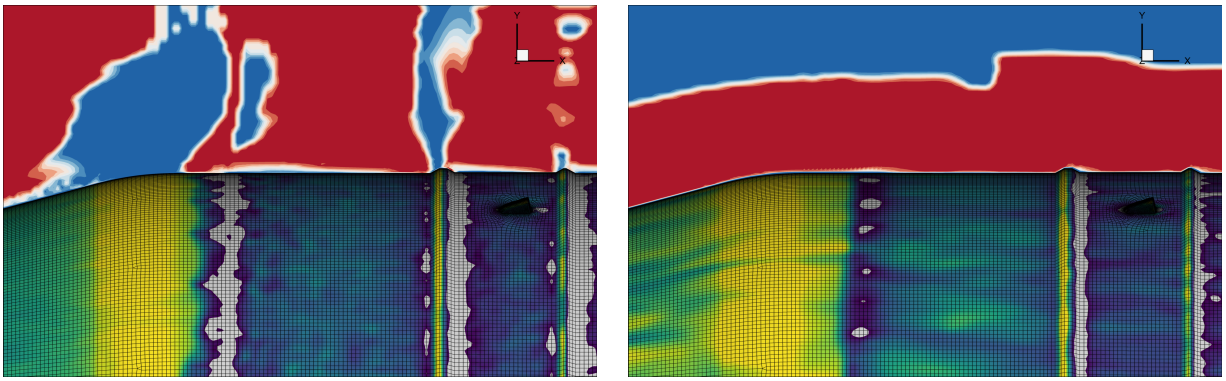

(a) DHRL shielding function (b) Nelson-Nichols shielding function

Figure 13: Saturated pseudocolor contours of the shielding function computed by each of the considered HRLES strategies. In all figures, red contours indicate LES-mode, blue contours indicate RANS-mode, and white contours represent the 'grey-zone' between RANS- and LES-modes.

While both methods predict a general LES region downstream of the USA shoulder, the DHRL shows more grey-zone behavior going deeper into the boundary layer than the Nelson-Nichols solution. This would allow more unsteadiness to be resolved, though it could be better resolved on a finer grid. While difficult to discern, the Nelson-Nichols solution shows blue contours representing an attached turbulent boundary layer along the entire length of the pictured geometry. Just downstream of the blue contours on the USA shoulder, the DHRL solution allows LES-mode and grey-zone behavior to penetrate all the way to the surface of the wall. This is seemingly key to predicting the location and intensity of the separation at this point. Again, a finer grid may replace more of the grey-zone behavior with pure LES-mode in this region and may move the DHRL solution to capture the current amplitude of the fluctuating pressure levels in this region. A fine grid is being considered to evaluate this hypothesis, but results are not ready for the current work.

3. Third-Octave Spectra

So far, qualitative comparisons have been made about the spatial extent of separation and reattachment, and quantitative comparisons were made about the fluctuating pressure levels within these unsteady regions. Perhaps equally as important as noise levels to vibroacoustic analysis is the distribution of the noise within the frequency domain. This section will present plots of power spectra density (PSD) that have been filtered into third-octave frequency bins. The filtering was conducted in order to overcome the disparate sample rate between the wind tunnel (very fast) versus the CFD data (relatively slow, $1/\Delta t$). In addition, the wind tunnel measurements were recorded for a significantly longer length of time than the length of the statistically stationary CFD simulation time interval ($\approx 1s$). Thus, the $x-$axes are truncated to only show frequencies which could be sufficiently well-resolved by the CFD. 'Well-resolved' is defined here as approximately an $\mathcal{O}(10^2)$ number of samples for the lowest frequency waves.

Before the PSDs are shown on a probe-by-probe basis, a global look is provided by plotting the third-octave spectra computed by every probes' time history on a single carpet plot in Fig. 14. In these spectrograms, the frequency, expressed as $St=f\,D_{AUAT}/U_{ref.}$ runs along the $y-$axis. The probe index ranging from 1 to the number of probes is plotted along the $x-$axis, though the indexing is ordered in terms of increasing streamwise position, reaching the aft end of the vehicle at the right end of the plot. Finally, the contour colors represent sound pressure level (SPL), blue being lower values and red being higher values. Wind tunnel probes with seemingly erroneous pressure time histories resulting in the measure of zero SPL are not omitted.

Clear horizontal lines are evident in Fig. 14a, these represent 'tunnel tones' that may be caused by various phenomena such as compressor blade passage, strut shedding tones, and the slotted tunnel walls. These two clear tunnel tones will be denoted as dotted vertical lines on every PSD moving forward for clarity. Just short of halfway along the $x-$axis, there is a vertical band of high SPL occurring across a broad range of Strouhal numbers. This is corresponding to the USA shoulder separation-reattachment system with the lower Strouhal number levels likely associated with the streamwise oscillation of the shock foot. Just past this system, elevated noise levels can be seen shifting to medium-to-high Strouhal numbers as the turbulent flow continues to convect

downstream and begins to interact with the circumferential flanges. Inspection of Fig. 14b again indicates that the Nelson-Nichols solution fails to capture any rise in pressure fluctuations near the USA shoulder, and the response to the flanges is muted. In addition, the high frequency 'roll-off' encroaches from the top of frame deeper than that from DHRL in Fig. 14c, especially where the USA shoulder shock system should have been predicted. Though as shown previously, both CFD solutions capture the SPL induced by the wake of the abort motors fairly well as is indicated by the elevated and fairly broadband noise levels on the left end of the plot. The spectrogram created by post-processing DHRL solution (Fig. 14c) again shows the ability to capture the spatial extent of the USA shoulder shock system and the associated increase in SPL at the correct frequency ranges, albeit at slightly lower values of SPL compared to the wind tunnel.

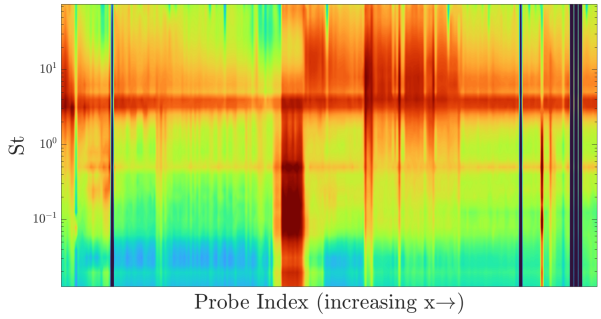

(a) Wind tunnel

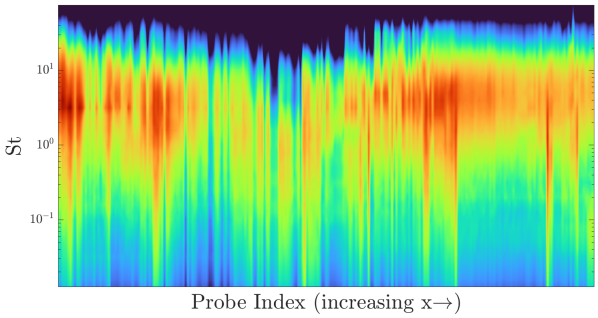

(b) Nelson-Nichols hybrid RANS-LES solution

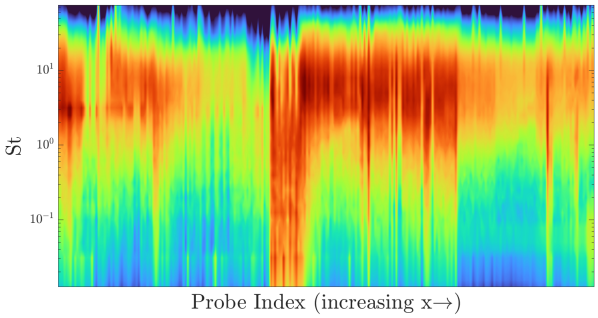

(c) DHRL solution

Figure 14: Spectrograms computed using data sampled (a) by Kulite® sensors for the wind tunnel and (b)-(c) at equivalent probe locations in the CFD simulations.

The analysis is completed by analyzing the third-octave spectra for a selection of probes. The first set of probes that are considered are those along a clocking-angle of ϕ=300°, directly behind one of the abort motors. These probes are visualized and given a local index in Fig. 15. The corresponding PSDs are shown in Figs. 16a-16f. Note that the shaded grey region represents acoustic 'doubling' to be used as an accuracy target for the CFD.

The probe with local index '1' is directly downstream of the abort motor wake, and both HRLES strategies are operating in virtually full LES-mode and capture the broadband nature of the wake noise well. There are still generally elevated noise levels as the wake convects over the SM panels. While both CFD methods again predict the levels and frequency distribution well, the Nelson and Nichols solution starts to show high-frequency roll of after $St \approx 3-4$ while the DHRL generally does not begin to roll of until $St \approx 10$. Probes 6 and 7 are located just upstream of and on top of a small protuberance representing a rear-ward facing camera. The DHRL solution does a great job at picking up the elevated noise levels in the upstream probe.

This analysis is repeated once more for $\phi = 180°$ as is shown in Figs. 17 and 18. Again, the CFD predictions at probe 1 capture the abort motor wake well. The USA shoulder separation-reattachment system is captured somewhere between probes 5 and 6, with probe 6 showing the large jump in noise levels at low St corresponding to the shock motion. Perhaps due to the relatively small simulation time length ($1s$), both methods under-predict

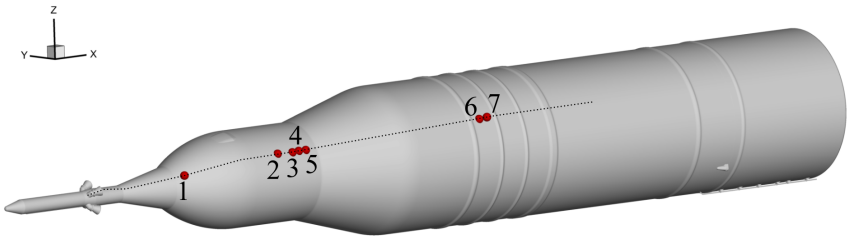

Figure 15: Annotated illustration of Kulite® sensors along a clocking-angle of ϕ=300°.

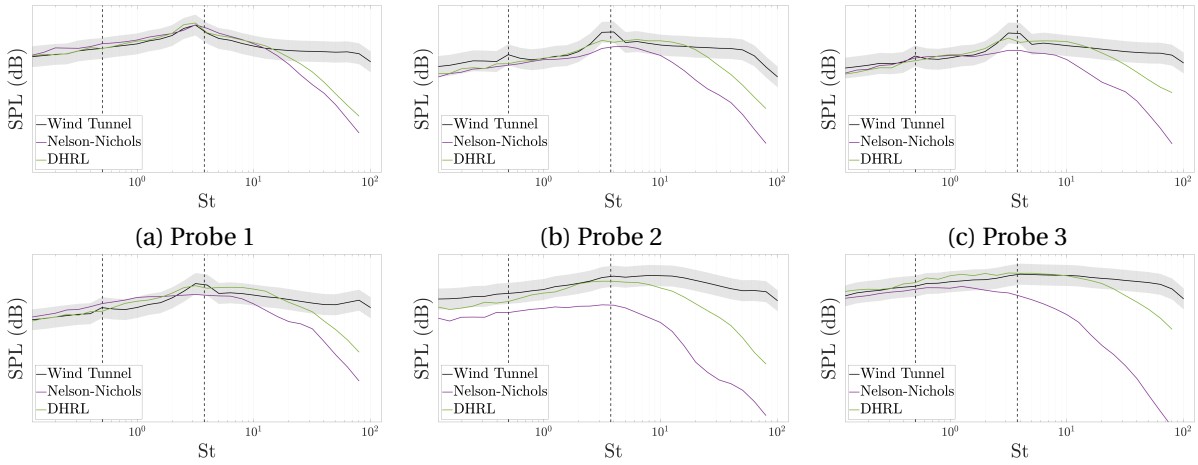

(a) Probe 1 (b) Probe 2 (c) Probe 3

(d) Probe 5 (e) Probe 6 (f) Probe 7

Figure 16: PSDs computed by wind tunnel and CFD data at the Kulite® sensors along a clocking-angle of ϕ=300°. The probe indexing is defined in Fig. 15.

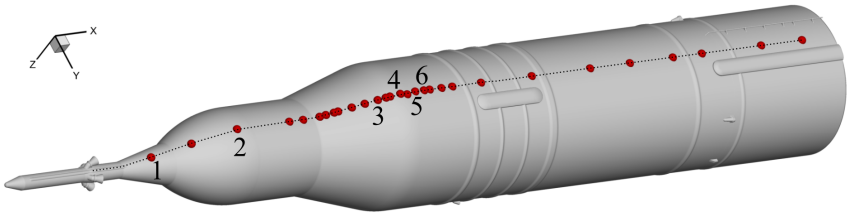

Figure 17: Annotated illustration of Kulite® sensors along a clocking-angle of ϕ=180°.

the noise in these low frequency ranges, but generally, the DHRL solution shows good agreement through the medium St range.

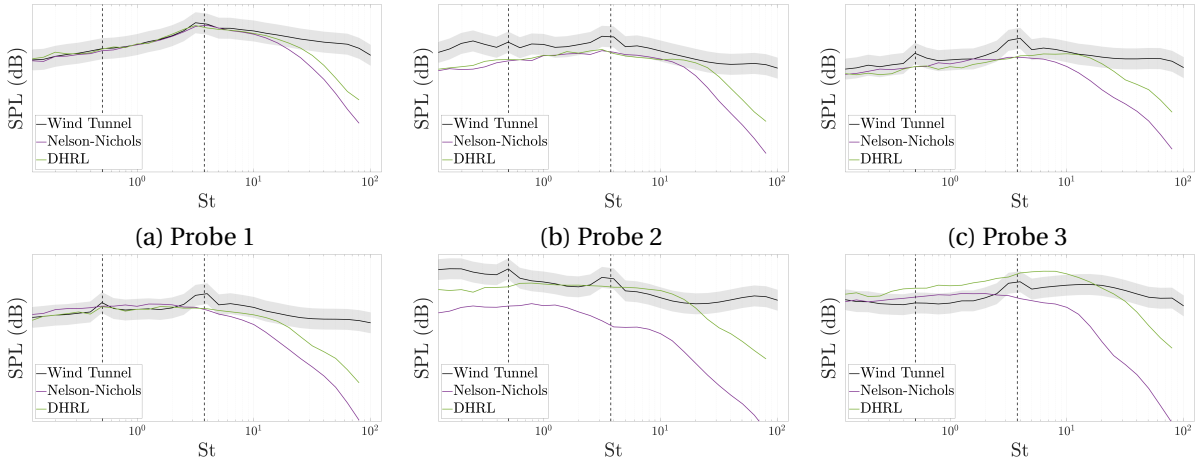

(a) Probe 1 (b) Probe 2 (c) Probe 3

(d) Probe 4 (e) Probe 5 (f) Probe 6

Figure 18: PSDs computed by wind tunnel and CFD data at the Kulite® sensors along a clocking-angle of ϕ=180°. The probe indexing is defined in Fig. 17.

4. *Discussion*

So far, CFD simulations conducted at $M = 0.84$ have been conducted with two HRLES strategies and compared to available wind tunnel data using qualitative analysis of shadowgraphs, surface pressure fluctuations, and spectrograms, and quantitatively by analysis of $c_{p,rms}$ and PSDs along constant clocking-angles. The DHRL method has shown through this analysis to capture the spatial extent of elevated and reduced noise levels very well. In the dominant region of the USA shoulder system, DHRL performed excellently by capturing the location of separation and reattachment, though slightly lower SPL values were predicted when compared to the wind tunnel data. This was found to be a combination of probe density near the USA shoulder and a delayed reaction of the shielding function to the separation, perhaps due to an insufficient amount of resolved LES-type content. The solution by the Nelson and Nichols method essentially did not predict any separation over the USA shoulder and generally predicted much lower SPL values over the entire surface compared to the wind tunnel. This is hypothesized to be due to the shielding function not switching from RANS-mode near interesting flow features. Perhaps again that additional resolved production would assist the shielding function in making the correct switch to LES. A refined grid will be considered in future works to evaluate these hypotheses.

B. Case 2: $M = 1.1$

The same simulation methodology and processes used for Case 1 is used here. Fig. 19 shows contours of CFL number on a cut-plane through the center of the domain at an instance in time from the DHRL simulation, the same timestep size of Δt=6.35 × $10^{-6}s$ is employed. Again, the LES simulations are started from a converged RANS flowfield, and sufficient time is allowed to convect any transients out of the domain before statistics are sampled. Due to time constraints, only $\approx 0.7s$ of simulation time are used for statistics for all cases, a fact that will be reflected in the lower bounds of the frequency domain plots in the coming sections. This section will advance similarly as the following section with the same analyses performed, though details may be omitted for brevity. Note that in this section, solutions obtained on a factor 2 refined grid are also presented along with the nominal grid solutions. For the fine grid solutions, the timestep width is not changed from Δt=6.35×$10^{-6}s$, thus the contour values in Fig. 19 would generally need to be multiplied by 2.

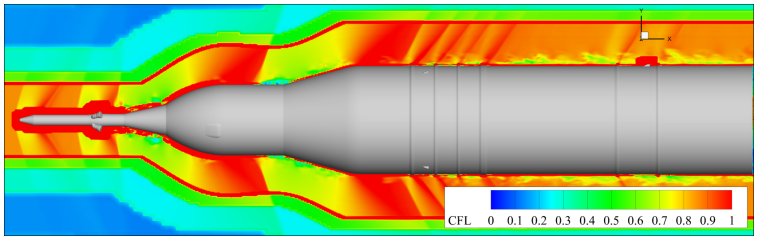

Figure 19: Contours of local CFL number shown on a cut-plane through the center of the domain obtained from an instance in time during the $M = 1.1$ DHRL simulation conducted on the nominal grid.

1. *Flow Visualization*

Color contours of Mach number are shown for the Nelson-Nichols and DHRL solutions in Fig. 20 for both grid densities. In contrast to the images shown in Fig. 7 for the $M = 0.84$ simulations, the primary flow features are now dominated by the SM panel-USA compression corner dynamics. The DHRL solutions generally resolve much smaller flow features in the USA compression corner region. In addition, the shocks that form on the circumferential flanges and their immediate wake are stronger in the refined DHRL solutions than the rest of the solutions. The cause of this is not immediately obvious, but it may be due to under-resolution in the flange region causing the other solutions to operate too much in RANS-mode until sufficient grid resolution is provided.

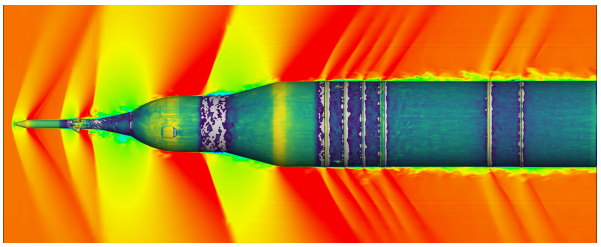

(a) DHRL, Mach number and $c_{f,x}$

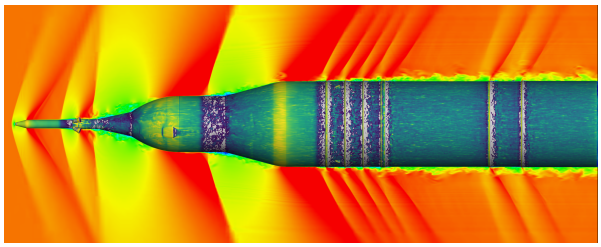

(b) DHRL refined grid, Mach number and $c_{f,x}$

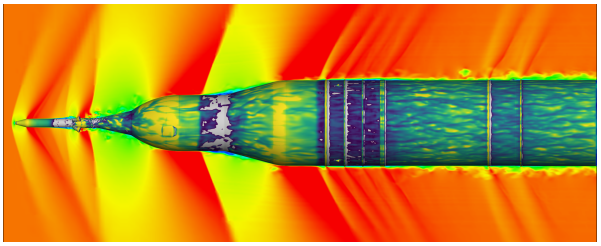

(c) Nelson-Nichols, Mach number and $c_{f,x}$

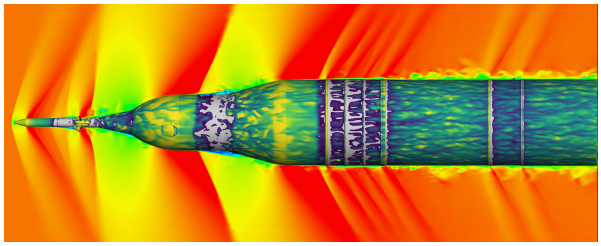

(d) Nelson-Nichols refined grid, Mach number and $c_{f,x}$

Figure 20: Saturated pseudocolor contours of Mach number shown on a cut-plane through the center of the domain at an instance in time from the DHRL and Nelson-Nichols HRLES simulations conducted at $M = 1.1$ on the (left column) medium grid and (right column) refine grid. Surface contours of skin friction coefficient 'blanked' for values less than zero are also shown on the body.

The fine grid DHRL solution in Fig. 20b shows a reduction in the level of separated flow in the compression corner when compared to its medium grid counterpart in Fig. 20a. This is perhaps simply due to further resolution of the energy cascade allowing eddies with higher wavenumbers to manifest and circulate in the separated flow. Comparison of the refined grid Nelson-Nichols solution with its medium grid counterpart, however, shows a small increase in the level of separated flow in this region - the same can be said for the circumferential flange region. It will become evident that Nelson-Nichols is undergoing model stress depletion (MSD) at the fine grid resolution. This is the result of the LES-mode penetrating too far into the inner layers of a low energy boundary layer, and it manifests as a sudden and nonphysical drop in shear stress at the wall - causing excessive flow separation.

2. RMS Sound Pressure

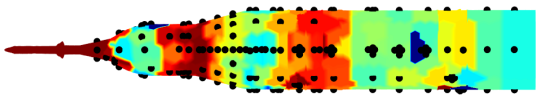

(a) OASPL, Wind tunnel

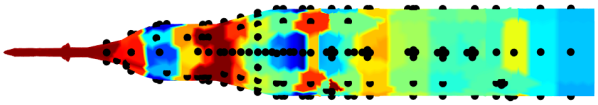

(b) OASPL Nelson-Nichols

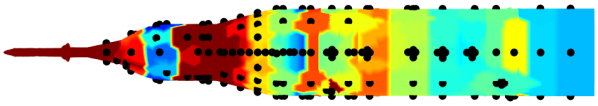

(c) OASPL Nelson-Nichols ref.

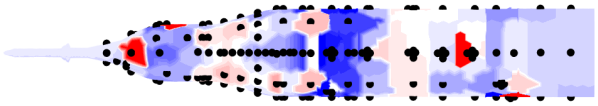

(d) ΔOASPL, Nelson-Nichols - Wind tunnel

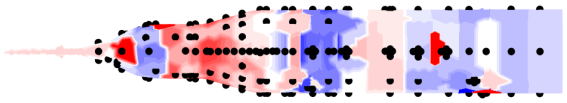

(e) ΔOASPL, Nelson-Nichols ref. - Wind tunnel

Figure 21: Contours of OASPL interpolated from Kulite® locations to the centroids of surface elements on a coarse AUAT mesh for the $M = 1.1$ (a) wind tunnel data and (b) nominal and (c) refined grid Nelson-Nichols solution. Images (d) and (e) show the interpolated values of ΔOASPL, indicating the difference between the CFD predictions and wind tunnel measurements of OASPL.

Values of OASPL are again interpolated from the Kulite® locations where they were sampled/computed to the centroids of surface elements on a coarse geometry mesh. Fig. 21 shows the result of the interpolation for the Nelson-Nichols solutions, and Fig. 22 shows the same for the DHRL solutions. All methods capture the general extent of the separation region induced by the USA compression corner dynamics, though both Nelson-Nichols solutions under-predict the noise levels generated in the flange region. The noise levels predicted by the fine grid Nelson-Nichols solution become very high in the compression corner region as is evident by the plot of $\Delta OASPL$ in Fig. 21 - again, due to assumed model stress depletion. Similar elevated noise levels are observed by the fine grid DHRL solution in the flange region, and the cause of this will be studied further in the coming analysis.

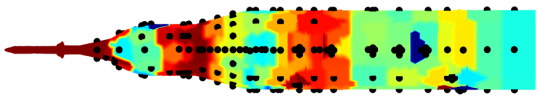

(a) OASPL, Wind tunnel

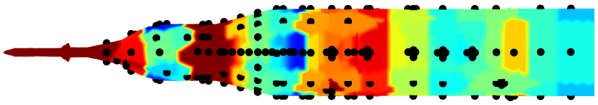

(b) OASPL, DHRL

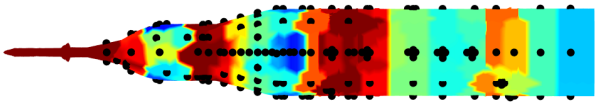

(c) OASPL, DHRL ref.

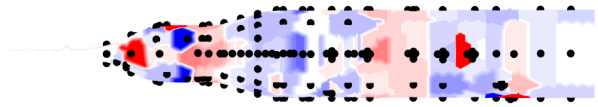

(d) ΔOASPL, DHRL - Wind tunnel

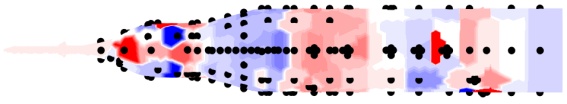

(e) ΔOASPL, DHRL ref. - Wind tunnel

Figure 22: Contours of OASPL interpolated from Kulite® locations to the centroids of surface elements on a coarse AUAT mesh for the $M = 1.1$ (a) wind tunnel data and (b) nominal and (c) refined grid DHRL solution. Images (d) and (e) show the interpolated values of ΔOASPL, indicating the difference between the CFD predictions and wind tunnel measurements of OASPL.

Inspection of Fig. 23, which plots $c_{p,rms}$ versus x-coordinate along constant clocking-angles, shows that the nominal grid Nelson-Nichols solution does an excellent job of capturing the fluctuating pressure levels in the USA compression corner and downstream of the flanges. Also evident is the over-prediction in the fine grid Nelson-Nichols case. The DHRL solutions show good agreement at both grid resolutions with a slight reduction in levels in the USA compression corner and elevated levels in the flange region for the refined solution.

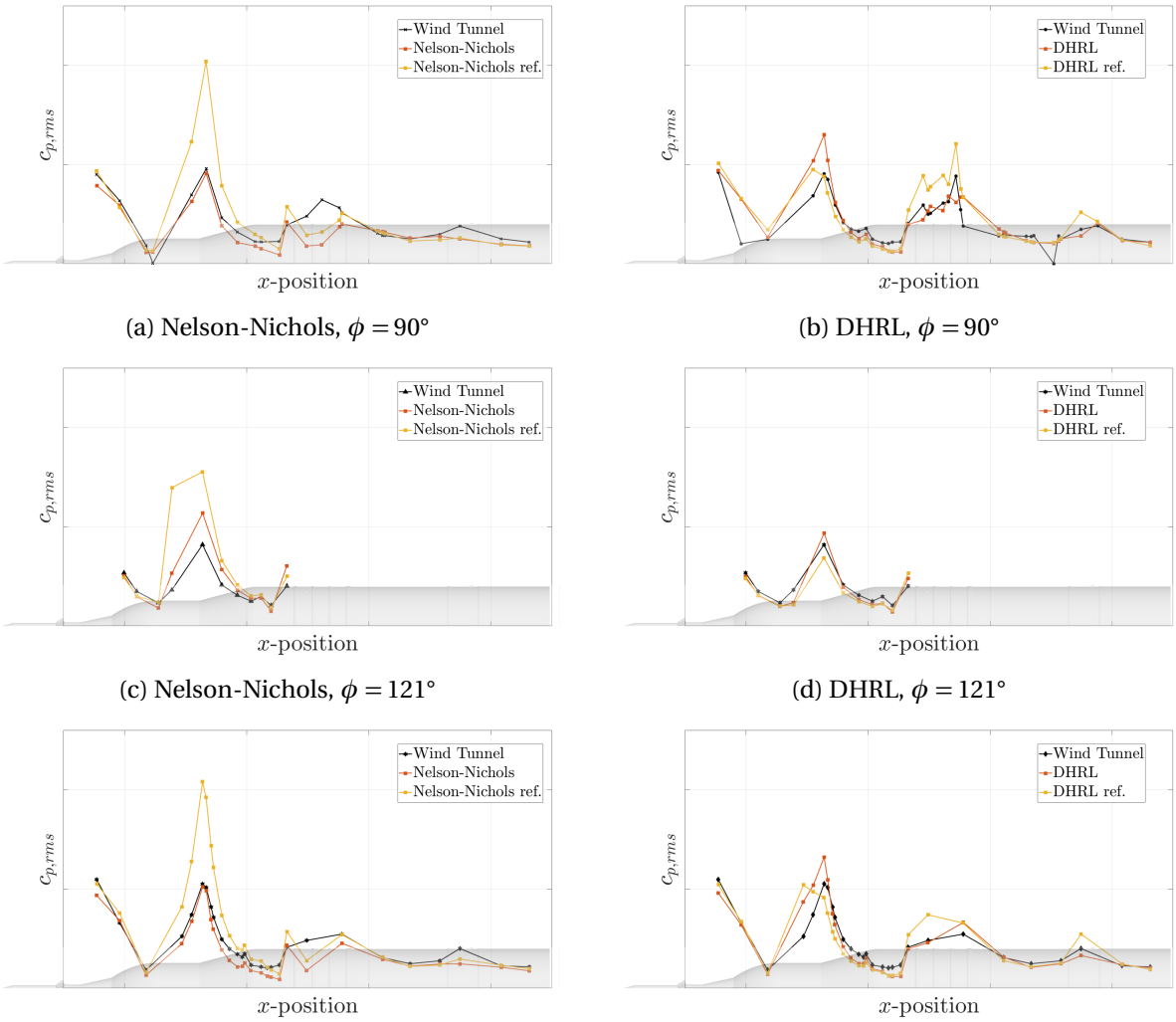

(a) Nelson-Nichols, $\phi = 90°$

(b) DHRL, $\phi = 90°$

(c) Nelson-Nichols, $\phi = 121°$

(d) DHRL, $\phi = 121°$

(e) Nelson-Nichols, $\phi = 180°$

(f) DHRL, $\phi = 180°$

Figure 23: Plots of $c_{p,rms}$ versus x-coordinate along various constant clocking-angles for the $M = 1.1$ case.

Before proceeding to the frequency analysis, the cause of the observed over-/under-predictions of $c_{p,rms}$ by the different grid solutions is sought in the contours of the shielding function for each case. The computed shielding functions are shown at an instance in time for each simulation in Fig. 24. As the Nelson-Nichols solution refines, there seems to be no major shift in the prediction of the LES and RANS regions which is surprising given the observed differences in the prediction of $c_{p,rms}$. The same can be said for the two DHRL solutions with the main differences occurring in the resolution of grey-regions, becoming smaller and allowing a quicker RANS-to-LES transition as the grid refines. This is good news for DHRL as the complex shielding function appears to remain agnostic to increasing grid refinement.

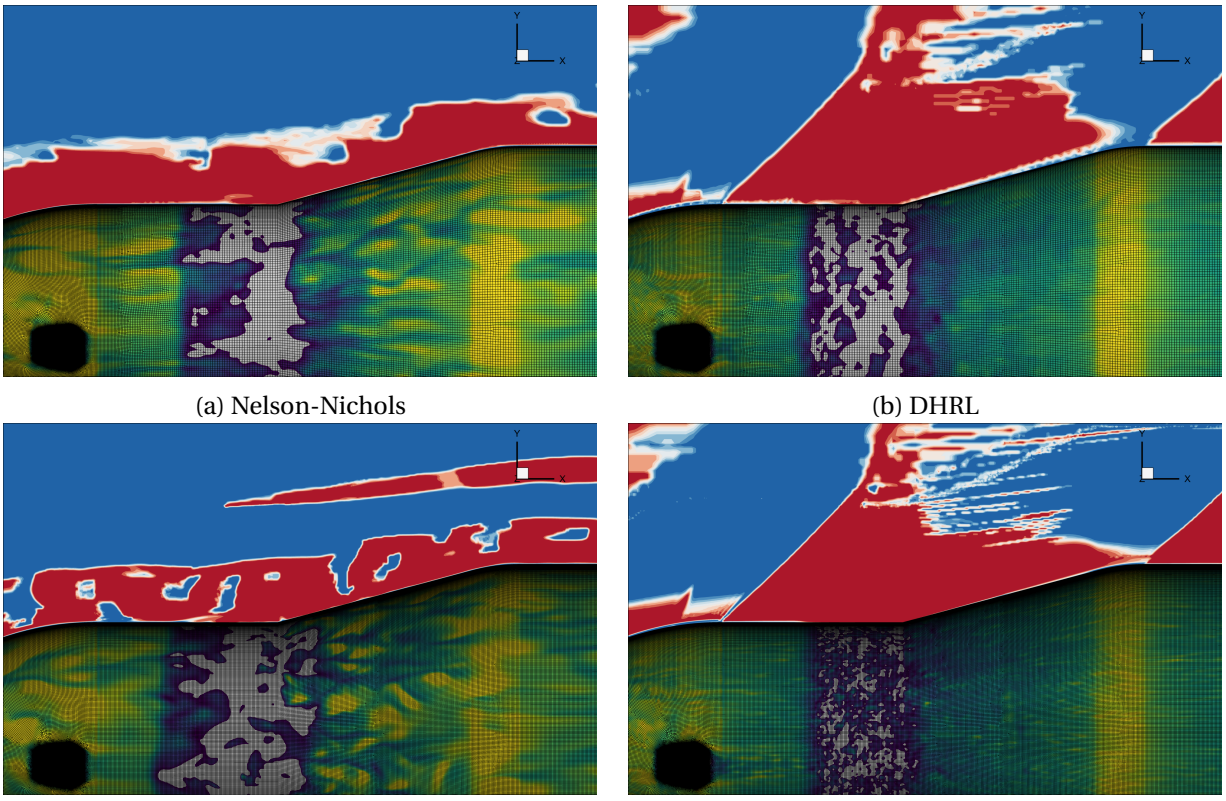

(a) Nelson-Nichols

(b) DHRL

(c) Nelson-Nichols ref.

(d) DHRL ref.

Figure 24: Color contours of the shielding function for the medium and refined grid solutions conducted at $M = 1.1$. Blue contours represent RANS-mode, red contours represent LES-mode, and white contours represent the 'grey-zone'.

3. *Third-Octave Spectra*

PSDs are computed along $\phi = 0°$ (see Fig. 25 for reference) and are shown in Fig. 26. The locally indexed probe 1 is directly between two abort motor nozzles, and the predicted noise levels for all simulations are consistently above the wind tunnel recordings. The cause of this is not immediately obvious but may be attributed to modeling or geometric errors causing the abort motor wakes to appear wider in the CFD simulations compared to what was observed in the wind tunnel, exposing the probe to a significant amount of LES content. One other observation that is immediately obvious is that the tunnel tones that are marked by the dashed vertical lines in all of the images in Fig. 26 are simply not loud enough at this Mach number to be observable. That is, the floor of the noise levels at $M = 1.1$ is generally higher than what was previously seen at $M = 0.84$.

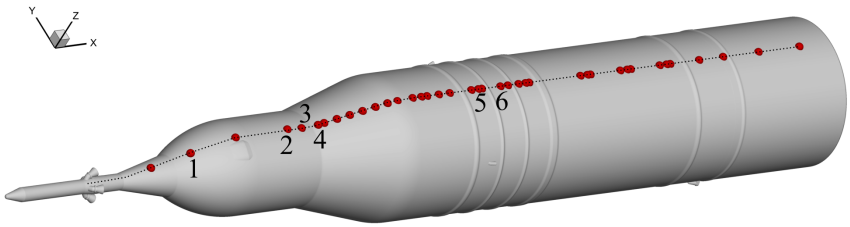

Figure 25: Annotated illustration of Kulite® sensors along a clocking-angle of ϕ=0°.

As the probes (with local index 2, 3, and 4) move into the compression corner system, the generally broadband nature of the noise levels is predicted well by all of the simulations, with the Nelson-Nichols simulations simply rolling off at lower St compared to the DHRL. There is still some over-prediction in the lower St number range by the CFD simulations, and this may be due to temporal errors caused by too large of a timestep or the length of the time integration window not being long enough and over-representing energy in the low frequencies. Finally, probes 5 and 6 are located in the flange region and show good agreement between all simulations and the wind tunnel data with the major differences occurring in the high St number range due to roll off. It is important to note, however, that these plots have the $y-$axis on a log-scale, and acoustic doubling is represented by the shaded grey region. Thus, while the simulations for Nelson-Nichols appear to agree better here than at $M = 0.84$, the fine grid solution routinely exceeds the acoustic doubling limit in these figures. Referring back to Figs. 23 also indicates a large over-prediction by the fine grid Nelson-Nichols solution, perhaps on the order of 2x. Despite this, all simulations appear to capture the general distribution of the energy in the frequency domain.

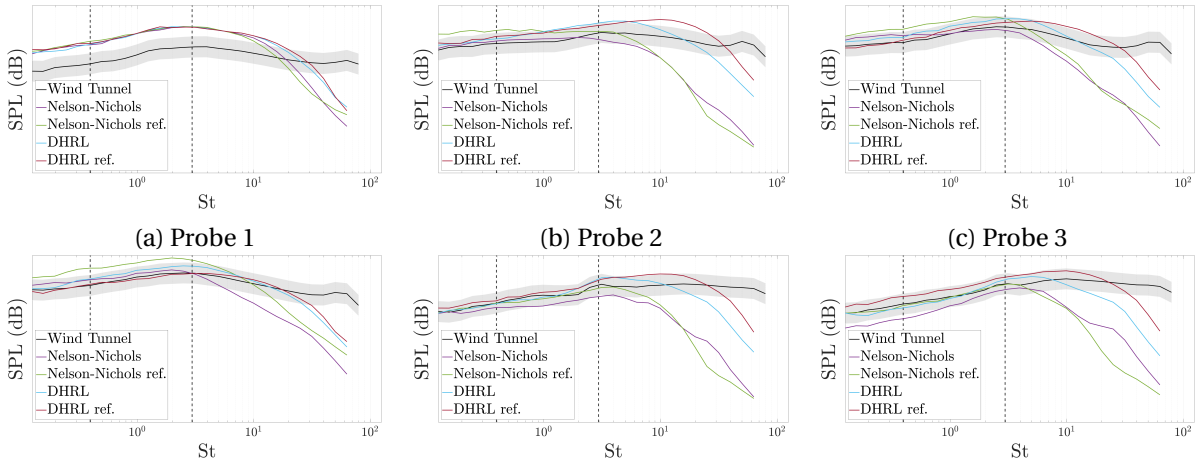

(a) Probe 1 (b) Probe 2 (c) Probe 3

(d) Probe 4 (e) Probe 5 (f) Probe 6

Figure 26: PSDs computed by wind tunnel and CFD data at the Kulite® sensors along a clocking-angle of ϕ=0°. The probe indexing is defined in Fig. 25.

4. *Discussion*

The noise levels observed at $M = 1.1$ are generally louder than those observed at $M = 0.84$. This rise in the noise floor washed out tunnel tones and created few regions where there was not appreciable noise levels. Thus, the CFD predictions were generally better across the vehicle. In some probes that were not presented, 'quiet' areas of flow showed large disagreement between the CFD and wind tunnel data due to a discrepancy in the ambient noise levels. While it seems that the medium grid Nelson-Nichols solution performed the best in terms of capturing the spatial extent amplitude of the elevated noise levels, the method is far too sensitive to increasing grid resolution as is evident by the drop in accuracy when considering the fine grid solution. Furthermore, despite good amplitude prediction, the method appears to blend too much RANS into the outer layer of the boundary layer and the near body, washing out unsteady content which causes an early roll off in the PSDs.

The DHRL solutions show good agreement at both grid resolutions. In fact, the DHRL method appears fairly insensitive to increasing grid refinement, at least within the levels considered in the present work. The differences between the methods arising due to increasing grid refinement are simply due to the nature of the methods' shielding functions. The Nelson-Nichols method contains no 'feedback' of the actual solution while the DHRL contains a contingency to only make the switch to RANS if the LES is capable of resolving the otherwise modeled stresses.

V. Conclusions

This paper demonstrated a need for high-fidelity, unsteady computational fluid dynamics simulations of aeroacoustic environments on NASA launch vehicles. Two hybrid RANS-LES schemes available in the Loci/CHEM solver[6,7] solver were introduced and evaluated, and the challenges associated with capturing convecting LES content through shocked flows were highlighted. The motivation to use a Cartesian-like, hexagonal-dominant grid type was also introduced. Grids of this nature are not only naturally suitable for LES, but for the monotone implicit LES (MILES) strategy used in this paper, they are desirable due to their low numerical dissipation.

The methods were first evaluated at $M = 0.84$, where an expansion-induced separation and reattachment system dominated noise levels on the test vehicle. In this case, the Nelson-Nichols scheme largely under-predicted the wind tunnel noise levels due to a general over-prediction of surface shear stresses causing the flow to stay attached as it expanded over the shoulder. The DHRL solution, however, showed good agreement in its ability to capture the location of the separation and reattachment point, but a small delay in the RANS-to-LES transition caused a under-prediction of peak noise levels in the system. It is thought that a refined grid would help the transition occur quicker, and thus elevate the peak predicted noise levels. Simulations studying this are currently underway and will be presented in future works. Finally, the distribution of the noise levels in the frequency domain was good for both methods despite the aforementioned differences in the predicted amplitudes.

At $M = 1.1$, the spatial extent and amplitude of the elevated noise levels was predicted excellently by Nelson-Nichols on the nominal, or medium level, grid. When a refined grid was considered, however, the predicted noise levels were generally too high compared to the wind tunnel. This was hypothesized to be due to model stress depletion, though no strong evidence for this was found. The DHRL solution performed well on both the medium and fine grids, which despite slightly worse performance compared to the medium grid Nelson-Nichols solution in terms of spatial extent and amplitude prediction, is perhaps an even more desirable feature. The ability of the DHRL shielding function to be fairly agnostic to increasing grid resolution increases confidence for when the method is applied to other more complex problems. In addition, the Nelson-Nichols solution generally blended too much RANS into the outer layers of the boundary layer and the unsteady near-wall flow, washing out LES content and causing an early frequency roll off in PSDs despite using the same timestep as the DHRL method.

Overall, the DHRL solutions appeared to agree best with wind tunnel data when all forms of analysis (flow field visualization, RMS sound pressure, frequency domain analysis) were aggregated. Due to its more complicated shielding function logic, the method is fairly insensitive to increasing grid resolution. The frequency domain analysis showed that the DHRL scheme also displayed good performance across the entire spectrum with notable high St number roll off. Future works will consider a refined grid on the $M = 0.84$ case as well as considering other geometries relevant for NASA aeroacoustics analysis, including the hammerhead Coe model. In addition, no effort was made in this work to ensure that the RANS-to-LES transition happened at a desirable y^+, and its possible some simulations occurred in a pure hybrid RANS-LES mode as opposed to a wall-modeled LES mode with RANS as the wall model. The effect of this, and of using locally unstructured/tetrahedral meshes around protuberances, will also be studied on more canonical and simple geometries such as flat plate turbulent boundary layers and compression corners.

VI. Acknowledgments

The authors would like to thank Dr. Christopher Morris from NASA's Marshall Space Flight Center for sharing his expertise with LES simulations using Loci/CHEM. The authors would also like to thank Dr. Michael Applebaum, Dr. Marc Eppard, and Bryson Frank from Mclaurin Aerospace for their contributions to fruitful discussions on meshing strategies and post-processing.

References

[1]Steva, T. B., Pollard, V. J., Herron, A., and Crosby, W. A., "Space launch system aeroacoustic wind tunnel test results," *AIAA Aviation 2019 Forum*, 2019, p. 3303.

[2]Cary, A. W., Chawner, J., Duque, E. P., Gropp, W., Kleb, W. L., Kolonay, R. M., Nielsen, E., and Smith, B., "Cfd vision 2030 road map: Progress and perspectives," *AIAA AVIATION 2021 FORUM*, 2021, p. 2726.

[3]Brauckmann, G. J., Streett, C., Kleb, W. L., Alter, S. J., Murphy, K. J., and Glass, C., "Computational and experimental unsteady pressures for alternate sls booster nose shapes," *53rd AIAA Aerospace Sciences Meeting*, 2015, p. 0559.

[4]Ramey, J. M., Giles, I. M., Goushcha, O., Heaney, P. S., Piatak, D. J., Sekula, M. K., and Soranna, F., "Parametric Study of the Forward Attachment Geometry for the Space Launch System Next Generation Booster," *AIAA SciTech 2023 Forum*, 2023, p. 0427.

[5]Larsson, J., Kawai, S., Bodart, J., and Bermejo-Moreno, I., "Large eddy simulation with modeled wall-stress: recent progress and future directions," *Mechanical Engineering Reviews*, Vol. 3, No. 1, 2016, pp. 15–00418.

[6]Luke, E. A., Tong, X.-L., Wu, J., Cinnella, P., and Chamberlain, R., "Chem 2: A finite-rate viscous chemistry solver–the user guide," *Mississippi State University, Mississippi State, MS, Tech. Rep*, 2004.

[7]Luke, E. A. and George, T., "Loci: A rule-based framework for parallel multi-disciplinary simulation synthesis," *Journal of Functional Programming*, Vol. 15, No. 3, 2005, pp. 477–502.

[8]Boustani, J., Barad, M. F., Kiris, C. C., and Brehm, C., "An immersed boundary fluid–structure interaction method for thin, highly compliant shell structures," *Journal of Computational Physics*, Vol. 438, 2021, pp. 110369.

[9]Boustani, J., Barad, M. F., Kiris, C. C., and Brehm, C., "An immersed interface methodology for simulating supersonic spacecraft parachutes with fluid–structure interaction," *Journal of Fluids and Structures*, Vol. 114, 2022, pp. 103742.

[10]Boustani, J., Cadieux, F., Kenway, G. K., Barad, M. F., Kiris, C. C., and Brehm, C., "Fluid-structure interaction simulations of the ASPIRE SR01 supersonic parachute flight test," *Aerospace Science and Technology*, Vol. 126, 2022, pp. 107596.

[11]Morris, C. I. and Luke, E., "Implicit Large-Eddy Simulations of Hot and Cold Supersonic Jets in Loci-CHEM," *AIAA Scitech 2020 Forum*, 2020, p. 1333.

[12]Marcum, D. L. and Weatherill, N. P., "Unstructured grid generation using iterative point insertion and local reconnection," *AIAA journal*, Vol. 33, No. 9, 1995, pp. 1619–1625.

[13]Marcum, D. L., "Unstructured grid generation using automatic point insertion and local reconnection," *The handbook of grid generation*, 1998, pp. 18–1.

[14]Spalart, P. R. and Streett, C., "Young-person's guide to detached-eddy simulation grids," Tech. rep., 2001.

[15]Menter, F. R., "Two-equation eddy-viscosity turbulence models for engineering applications," *AIAA journal*, Vol. 32, No. 8, 1994, pp. 1598–1605.

[16]Nelson, C. and Nichols, R., "Evaluation of hybrid RANS/LES turbulence models using an LES code," *16th AIAA Computational Fluid Dynamics Conference*, 2003, p. 3552.

[17]Bhushan, S. and Walters, D., "A dynamic hybrid Reynolds-averaged Navier Stokes–Large eddy simulation modeling framework," *Physics of Fluids*, Vol. 24, No. 1, 2012, pp. 015103.

[18]Walters, D. K., Shah, P., Berg, D., and Luke, E. A., "Investigation of dynamic hybrid RANS-LES modeling for compressible turbulent flows," *Thermal and Fluid Engineering Summer Conference, New York NY*, 2015.

[19]Deck, S. and Renard, N., "Towards an enhanced protection of attached boundary layers in hybrid RANS/LES methods," *Journal of Computational Physics*, Vol. 400, 2020, pp. 108970.